Plasma Chem Plasma Process (2006) 26:149–175
DOI 10.1007/s11090-006-9009-3

ORIGINAL ARTICLE

Comparative Study of Plasma Spray Flow Fields and Particle Behavior Near to Flat Inclined Substrates

C. W. Kang · H. W. Ng · S. C. M. Yu

Received: 24 November 2005/Accepted: 28 November 2005/
Published online: 7 April 2006

Abstract Numerical models have been developed using computational fluid dynamics (CFD) analysis program FLUENT V6.02© to investigate the effect of the substrate on the behavior of the plasma flow fields and in-flight particles. Simulations are performed for cases where flat substrates are either present or absent, for the former, the substrate is oriented perpendicularly or inclined to the torch axis. It is shown that although the presence of perpendicular or inclined substrate significantly influences the plasma flow fields at the vicinity of the substrate, the particle behavior remain relatively unaffected. The insignificant effect of the substrate on particle behavior is qualitatively verified by experimental observation using SprayWatch© imaging diagnostics equipment. Images captured by the equipment confirm that the particles travel through the plasma plume with high momentum and show no sudden change in their trajectories right before impacting the substrate. Both the numerical and experimental findings show that the freestream model is sufficiently detailed for future work of this nature.

Keywords Atmospheric plasma spray · CFD modeling · Particle behavior · Inclined substrate

Nomenclature

A	Cross section area (m^2)
B	Empirical constant ($=9.81$)
C_D	Drag coefficient
C_μ	Empirical constant ($=0.09$)
$C_{1\varepsilon}$	Empirical constant ($=1.44$)
$C_{2\varepsilon}$	Empirical constant ($=1.92$)
C_p	Specific heat capacity (J/kg K)
D	Diffusion coefficient (m^2/s)

C. W. Kang · H. W. Ng (✉)· S. C. M. Yu
School of Mechanical and Aerospace Engineering,
50, Nanyang Avenue, Nanyang Technological University, Singapore 639798
e-mail: mhwng@ntu.edu.sg

D_p	Particle diameter (m)
E	Arc voltage (V)
G_κ	Product of the eddy viscosity and viscous dissipation terms
H_f	Latent heat of fusion (J/kg)
h	Enthalpy (J/kg)
h	Heat transfer coefficient (W/m^2 K)
I	Arc current (A)
K	von Kármán constant (=0.42)
k	Thermal conductivity (W/mK)
m	Mass (kg)
n_p	Number of particles
p	Pressure (Pa)
P'''_{in}	Constant heat source (W/m^3)
$\dot{q}$	Heat flux (W/m^2)
S_ϕ	Source term
T	Temperature (K)
T_A	Plasma temperature at adjacent element to the wall (K)
T_b	Boiling point (K)
T_i	Turbulent intensity (%)
T_m	Melting point (K)
T_w	Substrate temperature (K)
t	Time (s)
$\boldsymbol{u}$	Velocity vector (m/s)
$\boldsymbol{u}'$	Velocity vector fluctuation (m/s)
U	Velocity magnitude (m/s)
U_A	Plasma velocity at adjacent element to the wall (m/s)
u, v, w	Velocity components in x, y and z directions, respectively (m/s)
V	Volume (m^3)
Y_n	Mass fraction
y	Distance from element to the wall (m)
y_A	Distance from adjacent element to the wall (m)

Subscripts

∞	Far field region
l	Laminar state
p	Particle
t	Turbulent state

Greek symbols

α	Thermal diffusivity (m^2/s)
ε	Turbulent kinetic energy dissipation rate (m^2/s^3)
η	Torch efficiency (%)
Γ_ϕ	Diffusion coefficient
κ	Turbulent kinetic energy (m^2/s^2)
κ_A	Turbulent kinetic energy at adjacent element to the wall (m^2/s^2)
μ	Dynamic viscosity (kg/ms)
ν	Kinematic viscosity (m^2/s)
ϕ	Process variable
ρ	Density (kg/m^3)

τ Shear stress (Pa)
τ_w Wall shear stress (Pa)
ς Liquid fraction

Dimensionless numbers
Pr Prandtl number: $Pr = \frac{\nu}{\alpha}$
Re Reynolds number: $Re = \frac{\rho u D}{\mu}$
Re_r Relative Reynolds number: $Re_r = \frac{\rho D_p(\boldsymbol{u}-\boldsymbol{u}_p)}{\mu}$
U^* Dimensionless mean velocity
y^* Dimensionless distance from element to the wall
y_T^* Dimensionless thermal sublayer thickness

1. Introduction

Plasma spraying is a group of processes in which finely divided metallic or non-metallic materials in molten or semi-molten state are deposited on prepared substrates to form a protective coating. It involves three separated but interrelated processes which are shown schematically in Fig. 1. They are plasma generation, plasma and particle interaction and coating formation. Numerous research on these three stages of plasma spraying have been published giving impetus to the continuous development of this field as reported in review papers by [1, 2]. Each of these areas involves substantial experimental and theoretical efforts.

In the past few decades, a number of numerical studies have been devoted to the modeling of the DC arc plasma spraying and interaction between the in-flight particles and the plasma jet [3–8]. Many workers [9–12] have investigated and showed that for typical plasma jet injection conditions, many operating parameters affecting heat, momentum and mass transfers between the plasma jet and the entrained particles. However, most of these efforts were conducted with the exclusion of substrate in the computational fluid dynamics (CFD) models for the sake of idealization simplicity [13–15]. It is understood that when the jet impinges on the substrate, there are reversals of gas flow around the obstacle in the gas path. The experimental measurement given in [16] indicated that the presence of the cooled substrate considerably increased the centerline plasma temperature by 22% at 5 mm elevation from the substrate surface. The understanding of substrate effects on plasma jet and particle behavior is therefore desirable to determine whether inclusion of substrate into CFD models is necessary for future studies.

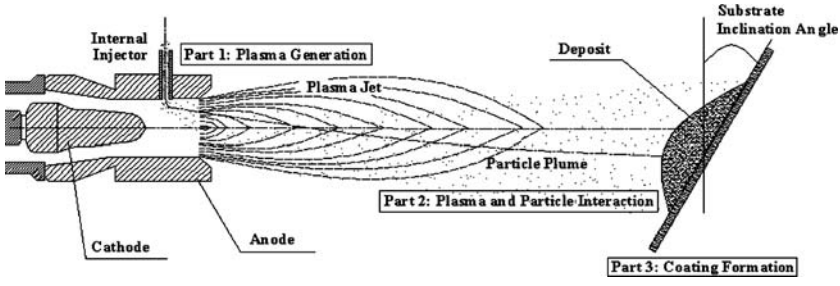

Fig. 1 Three separated but interrelated processes involved in plasma spray coating

The aim of the present work is to develop models representing the processes previously mentioned, i.e. plasma generation and plasma to particle interaction and investigates the effect on flow and particles due to the substrate. The three-dimensional CFD domain of the model encompasses the torch inlet, the air region in front of the torch and the solid obstruction of the substrate. The approach in modeling the plasma generation is by means of the conventionally adopted constant volumetric heat source model. The heat transfer from plasma to particles occurs in the air region and a one-directional coupling is adopted.

In order to compare the effects of substrate obstruction, three computational models are constructed:

(i) A 3D computational domain without the substrate,
(ii) The same above domain with the inclusion of substrate at a standard standoff distance of 80 mm in front of the torch and perpendicular to torch axis and
(iii) The same above domain with the substrate at 60° inclination to the vertical plane.

In addition, brief description on the experiment using SprayWatch© imaging diagnostics equipment is included in this paper. The SprayWatch© CCD camera is focused at the standoff distance of 80 mm where a substrate is either positioned or removed to capture the behavior of the in-flight particles under the influence of the substrate or in freestream respectively. When the substrate is present in the setup, it is either perpendicular or at 60° inclination. All the operation conditions of the experiments are replicated in the numerical modeling.

The complex surface geometry of real engineering spray parts can be considered to be comprised of multiple flat facets with each facet being flat and at individual inclination. The relevance of the inclined substrate in this work is to represent the facets in these multi-curvature surfaces. Discussion on the influence of the substrate on plasma flow fields and particle in-flight behavior are presented.

2. Modeling of plasma spray coating process

The geometry of the three models developed using the commercial software GAMBIT V2.04© (FLUENT Inc., 10 Cavendish Court, Lebanon, NH03766-1442.) are shown in Fig. 2(a, c, d); i.e. one without and two including the substrates. The cylindrical computational domain included the spray torch (diameter × length) $\phi 8 \times 10$ mm and free space in front of the nozzle for the plasma flame $\phi 160 \times 250$ mm. The substrates were $50 \times 50 \times 3$ mm (thickness). Dimensions of the torch were taken from the SG-100© model (Praxair Surface Technologies Inc., N670 Communication Drive, Appleton, Wisconsin 54915).

Simulation of plasma spray process consisted of two stages and was accomplished by commercial software FLUENT V6.02© (FLUENT Inc., 10 Cavendish Court, Lebanon, NH03766-1442.). In the first stage, a steady state thermal fluid solution for plasma and carrier gas flow without particle injection was obtained. The law-of-the-wall was utilized to account for the obstruction effect by the substrate towards plasma flow. In the second stage, particles were introduced as solid entities through internal injection port and the gas to particle heat and momentum transfer calculations were carried out for the pertinent particle parameters (such as temperature, velocity, size, number concentration and dispersion behavior). The plasma to particle interaction was considered one-directional, implying that the process of particle heating or cooling and acceleration or retardation took place from the plasma to particle but not in reverse. This was justified due to dilute particle flow (the ratio of volume of the particle

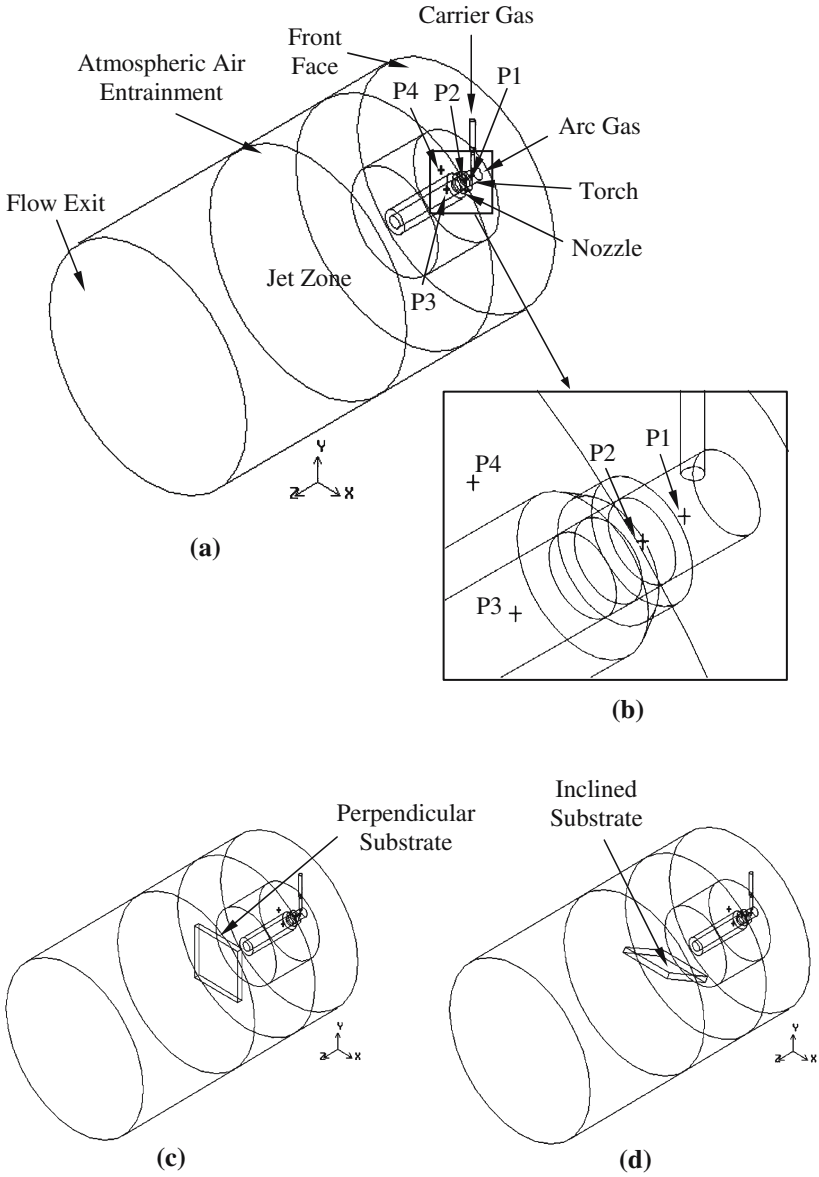

Fig. 2 Computational domains for internal injection plasma spraying. (**a**) Freestream model, (**b**) enlarged view for locations P1 to P4, at which plasma temperature and velocity were extracted for grid independence tests, (**c**) substrate model with perpendicular substrate and (**d**) substrate model with inclined substrate

to volume of the gas, was approximately 3×10^{-5}). The energy that the plasma received or gave to the particles was not significant enough to alter the plasma temperature and velocity.

2.1. Plasma heat generation

The heat generated by a high intensity electric arc was represented by a volumetric heat source. No swirl was present in the plasma heat generation since the SG-100© torch has

the primary gas injected normally from gas injector into the torch. The plasma plume was assumed as a steady state and incompressible gas. The assumption of incompressibility is validated by the calculation of Mach number and the procedure is attached in Appendix A. In addition, the plasma flame was assumed as optically thin and chemically inert with temperature dependent thermodynamic and transport properties in local thermodynamics equilibrium (LTE). The temperature dependent thermodynamic and transport properties for argon (used as primary and carrier gas) and air were adopted from [17] and input as a piecewise linear profile in FLUENT©.

2.1.1. Governing equations

The general form of governing differential equation for plasma flow is shown in Eq. (1). An example of the derivation of momentum equation in x direction is given in Appendix B.

$$\nabla \cdot (\rho \boldsymbol{u} \phi) = \nabla \cdot (\Gamma_\phi \nabla \phi) + S_\phi, \tag{1}$$

where ϕ is the process variable and $\boldsymbol{u}$ the velocity vector. The diffusion coefficients, Γ_ϕ and the source terms, S_ϕ for the different conservation equations are summarized in Table 1.

To account for the arc heating, the volumetric heat source was included in the governing energy equation and defined as in Eq. (2).

$$P_{\text{in}}''' = \frac{\eta E I}{V}, \tag{2}$$

where P_{in}''' is the volume-averaged heat source, E the arc voltage, I the arc current and V the volume of the anode. Torch efficiency, η, which takes into account for the heat loss mainly through cooling water in plasma torch was assumed to be 67% after [18].

2.1.2. Wall functions

Owing to the presence of the solid substrate, the flow behavior and turbulent structure are considerably different from the free turbulent flows. The mean velocity is at a maximum far away from the wall and sharply decreases in the near-wall region. High values of velocity fluctuations are found adjacent to the wall where the large mean velocity gradients ensure that turbulence production is high. To have an accurate representation of the flow in the near-wall region, semi-empirical formulas called wall functions were used to link the viscosity-affected region with the wall and the fully turbulent region.

Equations (3) and (4) show that the flow close to the wall is influenced by viscous effect and does not depend on freestream parameters. The plasma velocity at adjacent element to the wall, U_{A} strongly depends on the distance, y from the wall, plasma density, ρ and viscosity,

Table 1 The process variables, diffusion coefficients and source terms for Eq. (1)

Equation	Variable (ϕ)	Diffusion coefficient (Γ_ϕ)	Source term (S_ϕ)
Mass	1	0	0
Momentum	u, v, w	$\mu_{\text{l}} + \mu_{\text{t}}$	$-\nabla p$
Energy	h	$k_{\text{l}} + k_{\text{t}}$	P_{in}'''
Species	Y_n	$D_{\text{l}} + D_{\text{t}}$	0
Turbulence	κ, ε	$\mu_{\text{l}} + \frac{\mu_{\text{t}}}{Pr_{\text{t},\kappa}}, \mu_{\text{l}} + \frac{\mu_{\text{t}}}{Pr_{\text{t},\varepsilon}}$	$G_\kappa - \rho\varepsilon,\ C_{1\varepsilon}\frac{\varepsilon}{\kappa}G_\kappa - C_{2\varepsilon}\rho\frac{\varepsilon^2}{\kappa}$

μ and the wall shear stress, τ_w [19]. Equations (3) and (4) are called the law-of-the-wall for mean velocity and were used as the wall functions [20].

$$U^* = y^* \quad y^* < 11.225, \tag{3}$$

$$U^* = \frac{1}{K}\mathrm{In}(By^*) \quad y^* > 11.225, \tag{4}$$

where U^* and y^* are the dimensionless velocity and distance from the element to the wall, K the von Kármán constant (= 0.42), B the empirical constant (= 9.81).

U^* and y^* are defined as:

$$U^* = \frac{U_\mathrm{A} C_\mu^{1/4} \kappa_\mathrm{A}^{1/2}}{\tau_w/\rho}, \tag{5}$$

$$y^* = \frac{\rho C_\mu^{1/4} \kappa_\mathrm{A}^{1/2} y_\mathrm{A}}{\mu}, \tag{6}$$

where C_μ is the empirical constant (= 0.09), κ_A the turbulent kinetic energy at point A (near-wall element) and y_A the distance from point A to the wall.

Reynolds' analogy between momentum and energy transport gives a similar logarithmic law for temperature [21]. As in the law-of-the-wall for mean velocity, the law-of-the-wall for temperature employed in FLUENT© comprises the following two different laws:

(i) Equation (7) is the linear law for the thermal conduction sublayer where conduction is important [20].
(ii) Equation (8) is the logarithmic law for the turbulent region where effects of turbulence dominate conduction [20].

$$\frac{(T_\mathrm{w} - T_\mathrm{A})\rho C_p C_\mu^{1/4} \kappa_\mathrm{A}^{1/2}}{\dot{q}} = Pr\, y^* \qquad y^* < y^*{}_T, \tag{7}$$

$$\frac{(T_\mathrm{w} - T_\mathrm{A})\rho C_p C_\mu^{1/4} \kappa_\mathrm{A}^{1/2}}{\dot{q}} = Pr_\mathrm{t}\left[\frac{1}{K}\mathrm{In}(By^*) + P\right] \qquad y^* > y^*{}_T, \tag{8}$$

where T_A is the plasma temperature at adjacent element to the wall, T_w is the substrate temperature, C_p the plasma specific heat capacity, $\dot{q}$ the heat flux to the substrate, y_T^* the non-dimensional thermal sublayer thickness and Pr_t the Prandtl number: $Pr_\mathrm{t} = \nu_\mathrm{t}/\alpha_\mathrm{t}$

P was computed using the formula given in Eq. (9) by [22].

$$P = 9.24\left[\left(\frac{Pr}{Pr_\mathrm{t}}\right)^{3/4} - 1\right]\left[1 + 0.28\,\mathrm{e}^{-0.007 Pr/Pr_\mathrm{t}}\right]. \tag{9}$$

2.1.3. Operating and boundary conditions

The operating conditions as shown in Table 2 were set and maintained the same for the three models. The mass flow rates of arc gas and carrier gas were input at the inlets of the torch and injection port respectively. The radial and axial exit boundaries were selected a distance far away from the exit of the nozzle such that atmospheric boundary conditions were imposed there. The boundary conditions for the turbulence model at inlets of the torch and injection port were turbulence intensity and characteristic length. The turbulence intensities at arc gas and carrier gas inlets were calculated based on Eq. (10) as:

Table 2 Operating conditions for plasma spraying simulation

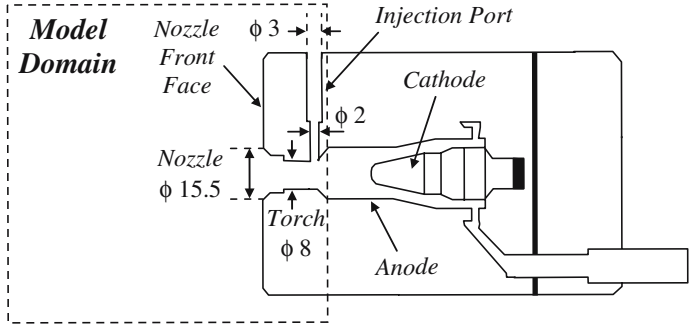

Operating condition/unit	Magnitude
Torch diameter/mm	8
Nozzle diameter/mm	15.5
Injection port diameter/mm	3
Powder size/μm	22–125
Current input/A	900
Voltage/V	35
Torch efficiency %	67
Heat source / W/m^3	4.4178×10^{10}
Arc gas flow rate (Argon Gas)/kg/s	1.9474×10^{-3}
Carrier gas flow rate (Argon Gas)/kg/s	1.136×10^{-4}
Turbulence intensity at arc gas inlet/%	4.83
Turbulence intensity at carrier gas inlet/%	6.09
Standoff distance (from nozzle front face)/mm	80

$$T_i = 0.16(Re_{\mathrm{HD}})^{-0.125}, \tag{10}$$

where Re_{HD} is the Reynolds number calculated for the gas flowing through the respective inlets, on the basis of the hydraulic diameter as the characteristic length.

2.1.4. Solution procedures

All the equations (mass, momentum, turbulence, energy and species) given earlier were solved by the FLUENT V6.02© commercial package using the control volume technique. This numerical approach stores scalar variables at the center of the control volume. The face values of scalar variables are also required for the convection terms and their values are gained from interpolation. First order upwind scheme was adopted to calculate the face values of the scalar variables since the problem was convection-dominated flow. For pressure and velocity coupling, the SIMPLE algorithm was employed [23, 24].

For the solution algorithm, the segregated solver was selected. This means that the segregated approach solves a single variable field by taking all control volumes at the same time into consideration. It then solves for the next field variable by again considering all control volumes at the same time and so on [20].

2.2. Particle dynamics and heat transfer formulation

Having obtained the converged solution for the plasma jet, particles were injected through the internal injection port and tracked throughout their flight within the computational domain. The particles were modeled in FLUENT© as discrete Lagrangian entities that received momentum and energy from the plasma in one-directional coupling. Particle in-flight behavior, i.e. particle velocities and particle temperatures were predicted based on the Newton second law of motion and from the energy balance equation, respectively.

In the particle dynamics formulation, it was assumed that the dominant driving force for particle acceleration was due to viscous drag force generated by the high speed plasma flow past the particles. In comparison, the force acting on a particle as a result of the existence of the temperature gradient (thermophoresis) is small and hence neglected. As for particle heating or cooling, convective heat transfer from plasma to particle and vice-versa was considered. The heating of particle by gas radiation was neglected as this effect is negligible compared to convective heat transfer to particles. In addition, the particle was assumed to have uniform temperature distribution by assuming perfect thermal conductance or zero thermal resistance. It is known that Zirconia has a finite thermal resistance, and a heat transport model which accounts for the heat flow into the particle would be more appropriate. However, this cannot be achieved at this time, due to the following reasons. There are approximately one million particles being injected in this study and it is not computational feasible to consider internal conduction for each individual particle. Secondly, the software capability are limited to perfect heat conductance within the particle and special codes needs to be developed for the predicting heat flow and resultant non-uniform temperature distribution internal to the particle. However, it is strongly believed that the conclusion of this paper with regard to the effect of substrate on particle trajectories will remain positive and will not be affected considerably even if the internal conduction is considered.

The Knudsen effect on particle acceleration and particle heating is only significant for very fine particles ($D_p < 10\,\mu\text{m}$). The smallest particle diameter involved in this study was $22\,\mu\text{m}$ and thus the Knudsen effect was neglected. In addition, the particle to particle interaction was assumed to be absent. Based on the calculation and chart provided by [25], the values of carrier gas and powder feed rate used in this study give mean distance between two particles approximately 10 times of their mean diameter which is sufficiently far apart for the avoidance of particle to particle interaction.

2.2.1. Governing equations

The momentum transport equation coupled with stochastic tracking determine the particle motion and trajectory. For particle heat transfer formulation, particle heating, cooling, melting and solidification are governed by the energy transport equation.

2.2.1.1. Momentum transport A force balance equation in Lagrangian reference frame equates particle inertia with viscous drag force acting on the particle,

$$\frac{\mathrm{d}\boldsymbol{u}_\mathrm{p}}{\mathrm{d}t} = F_\mathrm{D}, \tag{11}$$

$$\frac{\mathrm{d}\boldsymbol{u}_\mathrm{p}}{\mathrm{d}t} = \frac{3\mu C_\mathrm{D}(\boldsymbol{u} - \boldsymbol{u}_p)Re_\mathrm{r}}{4\rho_\mathrm{p} D_\mathrm{p}^2}, \tag{12}$$

where Re_r is the relative Reynolds number and C_D is the drag coefficient which are defined as follows:

$$Re_r = \frac{\rho D_p(\boldsymbol{u} - \boldsymbol{u}_p)}{\mu}, \tag{13}$$

$$C_D = a_1 + \frac{a_2}{Re_r} + \frac{a_3}{Re_r^2}, \tag{14}$$

where a_1, a_2 and a_3 are constants applicable for smooth spherical particles for a range of Reynolds number [20].

2.2.1.2. Stochastic tracking To account for the turbulence effect on particle trajectories, the "Random Walk Model" was utilized. In this model, the instantaneous value of fluctuating gas flow velocity was used and assumed to be isotropic and obey the Gaussian probability distribution [10, 20] so that;

$$\boldsymbol{u}' = \psi\sqrt{\overline{\boldsymbol{u}'^2}}, \tag{15}$$

where ψ is a normally distributed random number and $\sqrt{\overline{\boldsymbol{u}'^2}}$ is local root mean square (RMS) value of the velocity fluctuations. Thus, in Eqs. (12) and (13), instead of $\boldsymbol{u} = \bar{\boldsymbol{u}}$, the velocity fluctuation was included as $\boldsymbol{u} = \bar{\boldsymbol{u}} + \boldsymbol{u}'$.

2.2.1.3. Energy transport The concept of energy balance was adopted for convective and latent heat transfer from the surrounding plasma to the particle or vice versa.

For particle heating or cooling phase, the energy equation is as shown:

$$hA_p(T_\infty - T_p) = m_p C_p \frac{dT_p}{dt} \quad \text{for } T_p < T_m \text{ or } T_p > T_m. \tag{16}$$

The heat transfer coefficient, h in Eq. (16) was based on [26] correlation and is given in Eq. (17) [20].

$$h = \frac{k}{D_p}(2.0 + 0.6Re_r^{0.5}Pr^{0.33}). \tag{17}$$

As for particle melting or solidification, energy balance is defined as:

$$hA_p(T_\infty - T_p) = m_p H_f \frac{d\varsigma}{dt} \quad \text{for } T_p = T_m, \tag{18}$$

where ς is the liquid fraction.

2.2.2. Particle size distribution and properties

The commercially available powder 8% yttria-partially stabilized (Y_2O_3) zirconia (ZrO_2) ranged in size from 22 to 125 μm. The manufacturer's data in terms of diameter versus percentage weight was curve-fitted via a Rosin–Rammler distribution. This distribution represented particle diameter versus number from 22 to 125 μm in steps of 1 μm diameter was numerically introduced to the plasma flame through internal injection port with the rate of 9.6 g/min under the specified carrier gas pressure. In addition, the thermodynamics and transport properties for zirconia particle were required in the simulation and shown in Table 3.

Table 3 Thermodynamic and physical properties of yttria stabilized zirconia

Property	Value
Density ρ_p, kg/m^3	5890
Specific heat capacity C_p, J/kg K	*Eqn. below
Latent heat of fusion H_f, J/kg	7.06×10^5
Thermal conductivity k_p, W/mK	2.4
Kinematic viscosity ν_p, m^2/s	6.5×10^{-6}
Melting point T_m, K	2988
Boiling point T_b, K	5273

* For $273 < T_p < 873$ K
$C_p = 1.06343 \times 10^{-6} T_p^3 - 2.188953 \times 10^{-3}\ T_p^2 + 1.709671 T_p + 1.466367 \times 10^2$
For $T_p > 873$ K $C_p = 678.5$

Table 4 Temperatures, T (K) and velocity magnitudes, U (m/s) at monitoring points for (**a**) freestream, (**b**) perpendicular substrate and (**c**) inclined substrate models at increasing level of mesh refinement

Point	P1		P2		P3		P4	
	T (K)	U (m/s)	T (K)	U (m/s)	T (K)	U (m/s)	T (K)	U (m/s)
(a) *Freestream Model*								
Coarse (255226)	9767.86	828.44	11399.90	1079.48	412.39	8.25	300.00	4.63
Medium (439463)	9639.48	811.32	11484.40	1099.80	407.08	7.83	300.00	4.64
Fine (642802)	9598.04	807.05	11501.10	1108.32	405.65	7.85	300.00	4.67
(b) *Perpendicular Model*								
Coarse (261600)	9767.85	828.45	11400.20	1079.59	415.91	8.26	300.00	4.65
Medium (402881)	9717.41	821.49	11471.30	1095.83	406.94	7.82	300.00	4.63
Fine (587424)	9640.28	811.32	11495.00	1106.52	409.74	7.88	300.00	4.65
(c) *Inclined Substrate Model*								
Coarse (264311)	9767.85	828.45	11400.10	1080.02	434.44	8.29	309.47	4.66
Medium (456843)	9639.48	811.32	11484.40	1099.76	405.97	7.82	300.00	4.64
Fine (667289)	9598.04	807.05	11501.10	1108.30	406.26	7.86	300.00	4.64

Numbers in brackets indicate the number of elements

3. Grid independence tests

A series of grid independence tests was conducted on the mesh models at the beginning of the simulation process to ensure that optimized computational mesh was obtained. For the three models (freestream, perpendicular and inclined substrate models), grid independence tests have to be carried out for each mesh model. During the tests, the models were executed and the plasma temperature and velocity magnitude were extracted from four reference points to monitor the effects of the mesh refinement. The coordinates (X, Y, Z) of the selected points as indicated in Fig. 2(b) are P1 (0, 0, 0.005 m), P2 (0.002, 0.002, 0.012 m), P3 (−0.005, −0.005, 0.02 m) and P4 (−0.008, 0.008, 0.022 m). These points were selected because they were in the active zone of computation where high gradients of temperature and velocity existed. The results of grid independence tests for the three models are shown in Table 4.

For each model, three levels of refinement were considered, the coarse, medium and fine refinements, each having the number of elements which were in the ratio of 1×, 2× and 3× the number of elements of the coarse model respectively. For the four points, comparison of the temperatures and velocities between coarse and medium refinement models has an average of 3% difference. As for comparison amongst coarse and fine models, an average of 3% percentage difference is also noted. Doubling or tripling the number of elements only improves the percentage difference by 3% and therefore, the following coarse mesh models having 255,226 elements, 261,600 elements and 264,311 elements, respectively are adequate.

4. Results and discussion

4.1. Comparison of Plasma Temperature

In order to verify the author's numerical work, a model for torch with 6 mm nozzle diameter and 10 mm length as given by [27] was generated. This model was simulated based on the operating conditions of 10.8 kW power input and 40 L/min of argon gas flow rate. The mathematical models, the assumptions and the volumetric heat source approach remained the same as discussed earlier.

Figure 3(a, b) show the comparison of the author's numerical results and experimental measurements from [27]. The comparisons were carried out for the temperature distributions along the Y direction at two axial distances from the nozzle exit; i.e. $Z = 5$ mm and $Z = 15$ mm. It is noted that for both cases, the temperature distributions along the Y direction are predicted well by the author's numerical model. At 5 mm from nozzle exit, less turbulence intermingling between the plasma flow at the core region and the ambient air results in the planar profile, with maximum computed plasma temperature of 10174.8 K while the experiment shows 11,700 K (as encircled in Figure 3(a)). A maximum percentage difference of 13% is calculated from Eq. (19). Further downstream till 15 mm from nozzle exit, vigorous mixing decays the maximum plasma temperature till 5083.39 K for computation and 5920 K for experiment (as encompassed in Fig. 3(b)). The maximum percentage difference is 14%.

$$\text{Percentage difference} = 100^{*}\text{ABS}[(\text{Simulation} - \text{Experiment})/\text{Experiment}] \quad (19)$$

The maximum percentage differences for both cases are within the acceptable range for plasma spray modeling. This implies that the mathematical models applied, the assumptions made and the approaches utilized in this study in predicting the plasma temperature are reasonable.

4.2. Plasma flow fields

Figures 4 and 5 show plots of plasma temperature and velocity contours in the vertical symmetry plane (YZ) for perpendicular and inclined substrate models respectively. Figures 4(a) and 5(a) show the temperature and velocity contours of the freestream model in which the positions of the substrates can be imagined to be in the dotted space.

It is noted that the contours are not symmetrical about the torch axis, the reason is due directly to one-port carrier gas injection. The injection of carrier gas in the negative Y direction causes a slight divergence of plasma plume in the same direction.

Comparing the freestream and substrate results, the maximum values of plasma temperature and velocity exist at the upstream end of the plasma flow fields remain unaffected by the substrate as it is located at standoff distance of 80 mm which is too far from the torch to have any effect. It is noted that significant flow divergence occurs at the vicinity of the substrate. The substrate causes the plasma plume in the near-field region to spread radially outwards upon impinging the substrate.

More detailed views of the flow in terms of plasma velocity vectors are shown in Fig. 6. At the near-field region, the perpendicular substrate obstructs and diverts the flow into the directions towards the upper and lower parts of the substrate as well as in the radial direction. The plasma plume is deflected by the inclined substrate to flow along its surface towards the upper part of the substrate only.

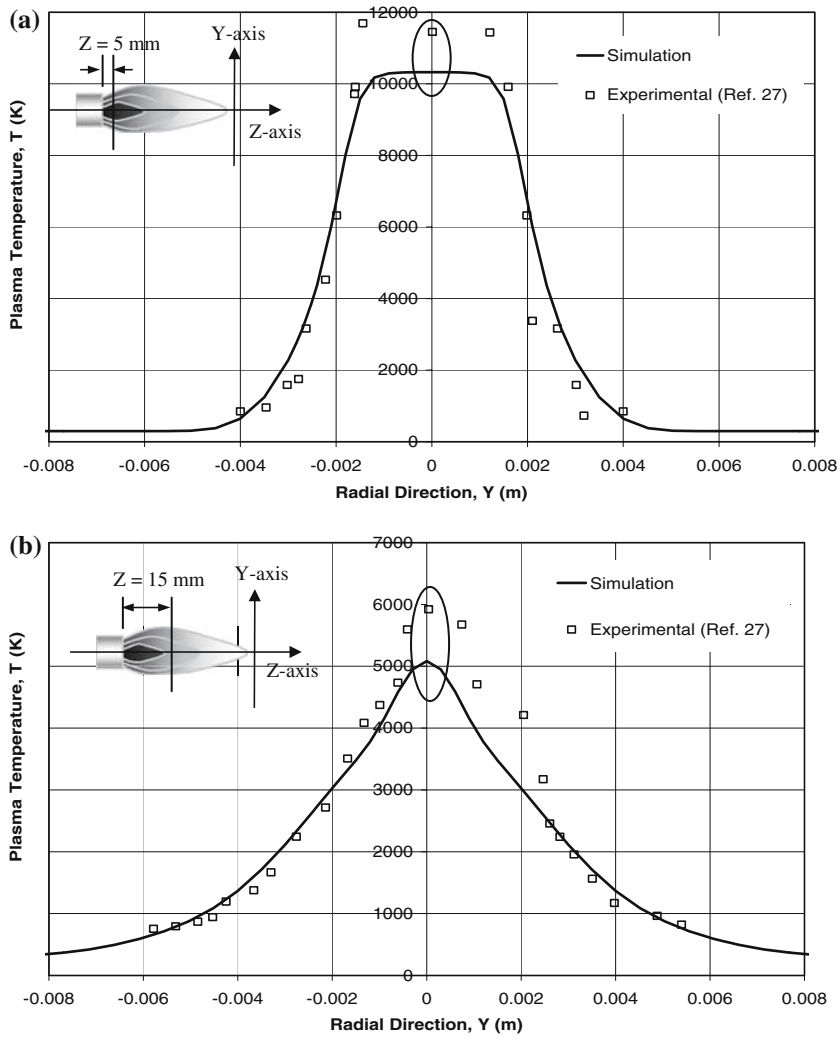

Fig. 3 Comparison of plasma temperature distributions for the case where power input, 10.8 kW and argon flow rate, 40 l/min at (**a**) 5 mm and (**b**) 15 mm from nozzle exit. Largest discrepancy between experiment and simulation was encircled

Figure 7(a,b) shows the temperature and velocity variations along the centerline (axis) for the three cases, respectively. Initially, the plasma temperature increases rapidly inside the torch due to heating by high intensity arc. The high temperature leads to the expansion of argon gas and with constant mass flow rate; plasma velocity is subsequently increased as can be seen in Fig. 7(b). For approximately 20 mm in front of the nozzle front face, the temperature and velocity show only slight reduction. Beyond this region, dramatic drops in plasma temperature and velocity to ambient condition are observed. Near the torch exit, the plasma jet maintains its original speed and forms a core region. Surrounding the core will be the mixing layers where the plasma jet mixes with the ambient stagnant air. At the end of

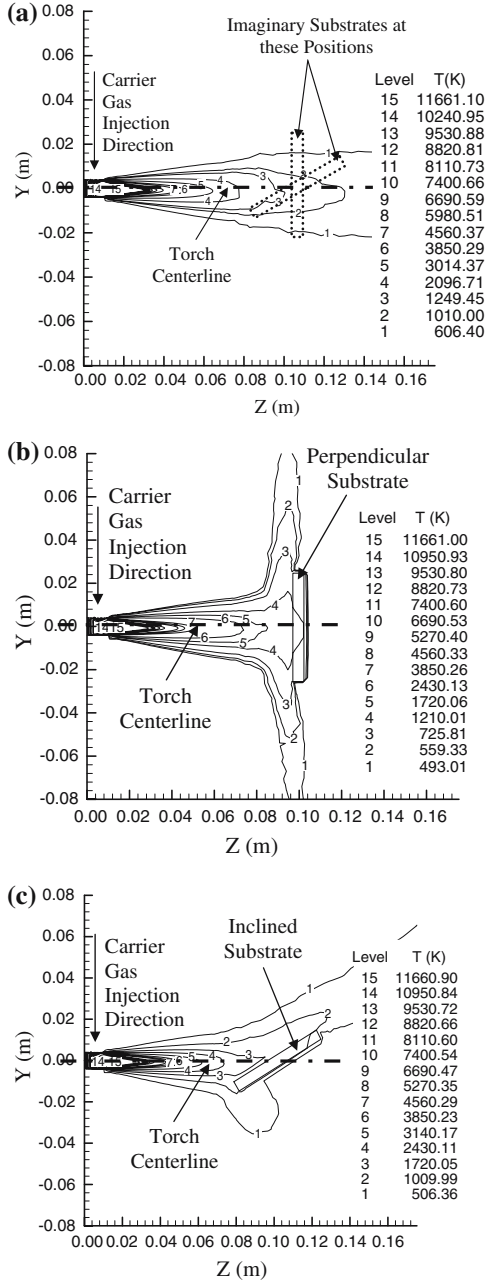

Fig. 4 Comparison of plasma temperature contours for (**a**) freestream, (**b**) with perpendicular substrate and (**c**) with inclined substrate in Y–Z plane

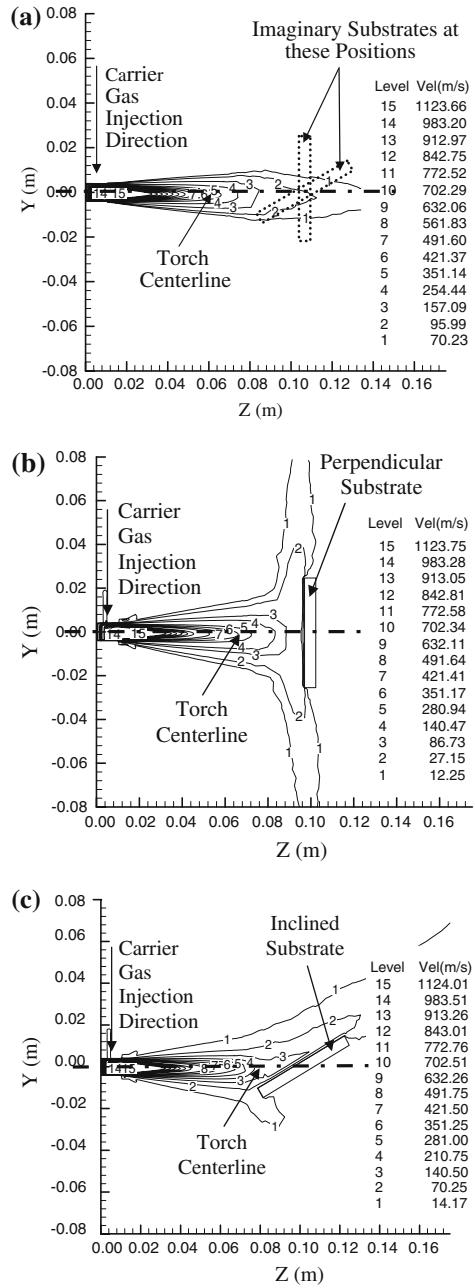

Fig. 5 Comparison of plasma velocity contours for (**a**) freestream, (**b**) with perpendicular substrate and (**c**) with inclined substrate in Y–Z plane

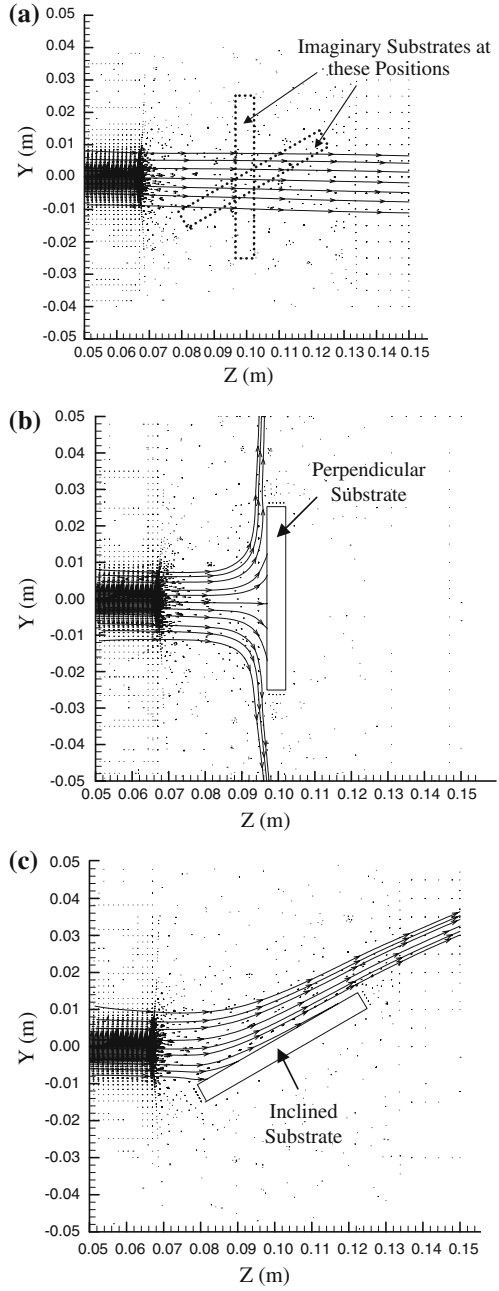

Fig. 6 Plasma velocity vectors for (**a**) freetream, (**b**) perpendicular and (**c**) inclined substrates in Y–Z plane

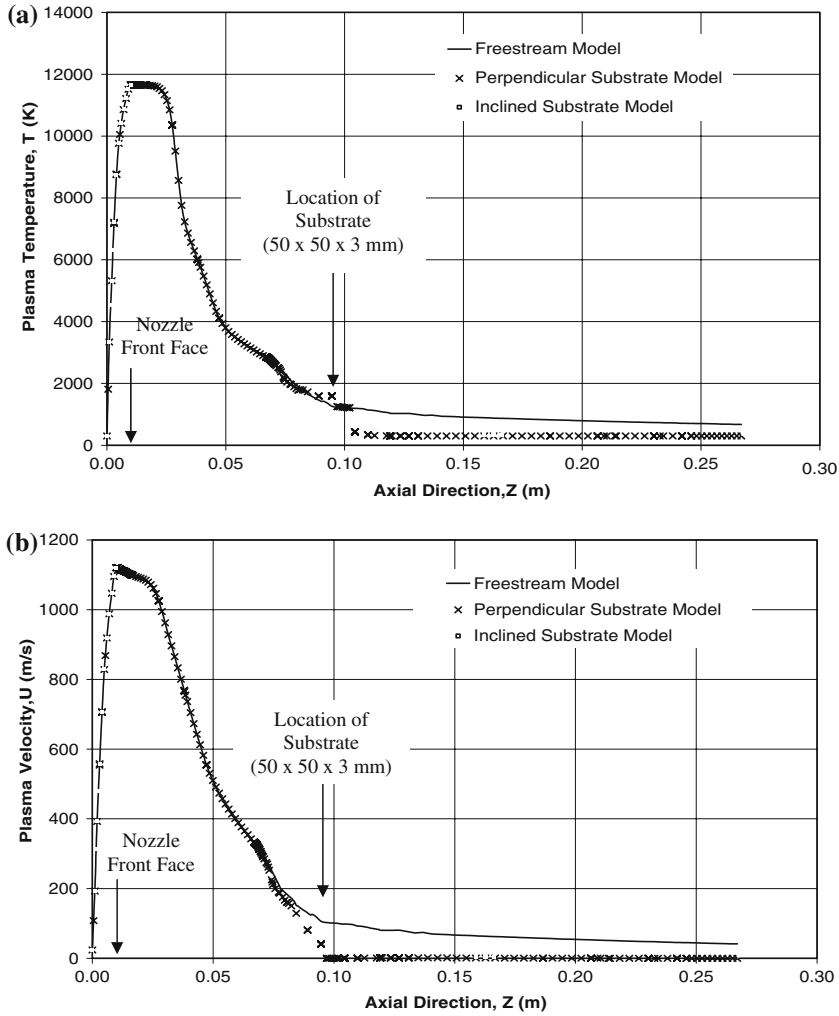

Fig. 7 Prediction of centerline axial distributions of (**a**) plasma temperature and (**b**) plasma velocity for freestream, perpendicular and inclined substrate models

20 mm distance, the surrounding mixing layers will merge, resulting the decaying of plasma velocity and temperature.

It is seen that regardless of whether the substrate is present, plasma temperature and velocity reduce at the same rate. In the far field region away from the substrate, for freestream and substrate models, the plasma temperature and velocity merge into one another. This indicates that the range of influence of substrate on plasma temperature and velocity is short and only occurs in its vicinity, approximately 5 mm in front of inboard face, i.e. surface facing towards the flow of the substrate.

Figures 8 and 9 show in detail the plasma temperature and velocity at the substrate along the surface as measured from its center (coordinates $X, Y = 0, 0$). The temperature and velocity plots are for the two parallel planes above the substrate's surface; at an elevation of 5 mm and at a much lower elevation of 0.1 mm. The 5 mm elevation is chosen because above

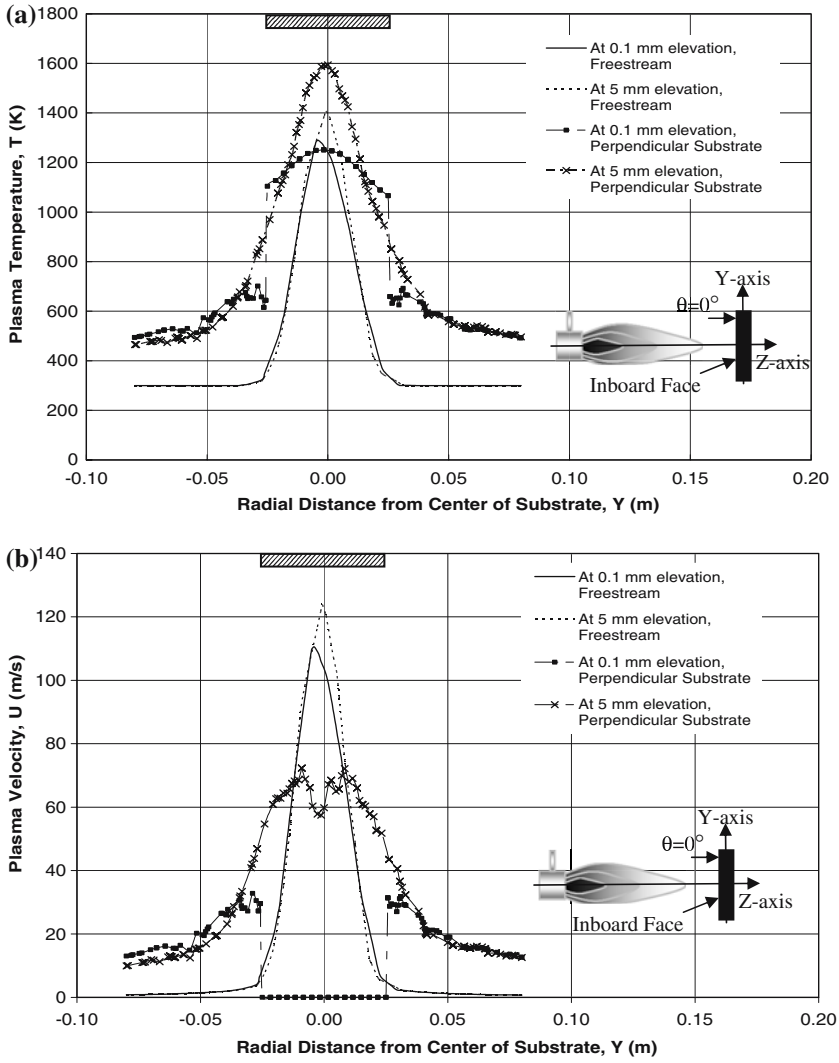

Fig. 8 (**a**) Plasma temperature and (**b**) plasma velocity radial distributions at 0.1 and 5 mm elevations above the surface of the substrate for freestream and perpendicular substrate models in Y–Z plane

this elevation, the plasma velocity and temperature remain largely unaffected by the substrate when compared to the freestream values. At the lower elevation, more drastic interferences are seen. The distortions in the shapes of the curves at 0.1 mm elevation are apparent in both the perpendicular (Fig. 8) and inclined (Fig. 9) substrates. For convenience the physical length of the substrates are also shown along the X-axis of the plot.

In Figure 8(a,b), the perpendicular substrate spreads the plasma plume and consequently results in wider radial distribution of plasma temperature and velocity. At 5 mm elevation, the substrate model tends to have higher plasma temperature than that of the freestream model, as shown in Fig. 8(a). This is because under the near stagnation condition, there is a blowback of gas from the substrate. At close proximity to the surface (elevation of 0.1 mm), heat conducts

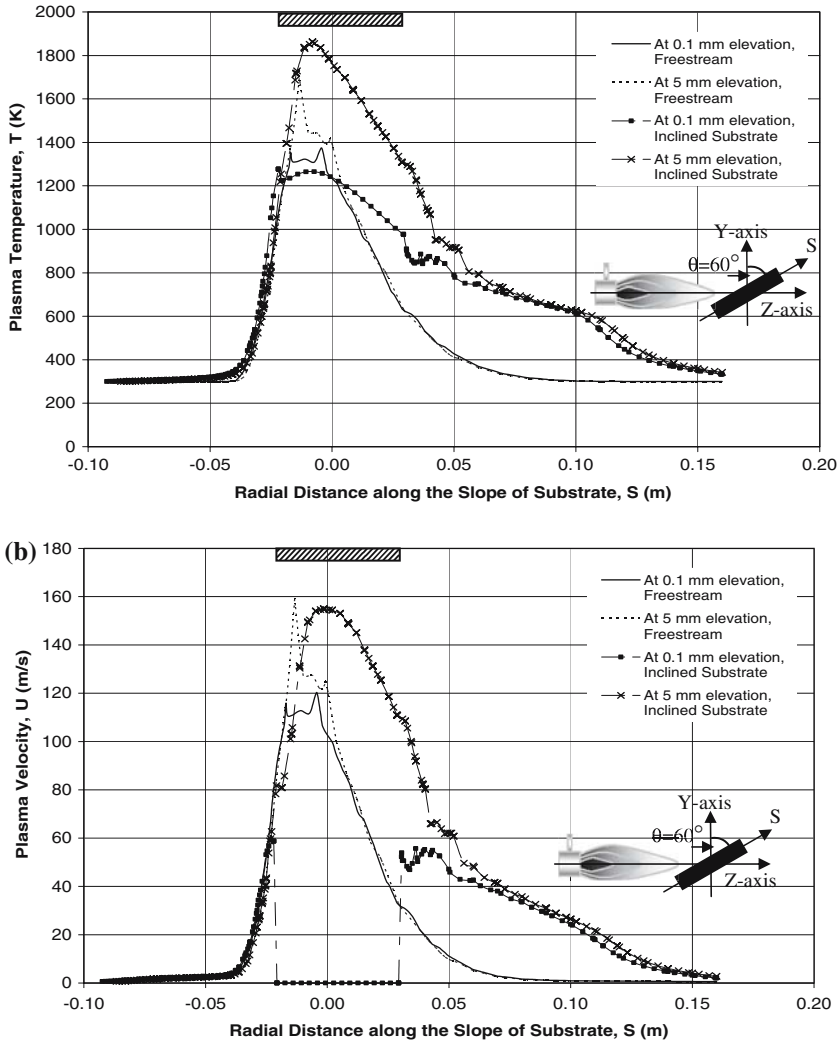

Fig. 9 (**a**) Plasma temperature and (**b**) plasma velocity radial distributions at 0.1 and 5 mm elevations above the surface of the substrate for freestream and inclined substrate models in $Y-Z$ plane

through the substrate and reduces the plasma temperature of substrate model compared to the freestream model. As for plasma velocity distribution in Fig. 8(b), the substrate surface retards the plasma velocity to stagnation condition, hence a zero plasma velocity along the substrate at inboard face is observed.

For the inclined substrate, the standoff distance is 80 mm from nozzle front face to the center of the substrate. Due to the incline, the lower half of the substrate has a smaller standoff distance while the upper half's standoff distance will be greater than 80 mm. The lower half of the substrate experiences higher temperature and velocity because of closer proximity to the torch and it guides the flow along the surface of the inclined substrate. Consequently, as can be seen in Figs 9(a,b), at 5 mm elevation, increases in plasma temperature of 400 K and velocity of 40 m/s compared to the freestream condition at the substrate center are noted.

4.3. Particle behavior

The in-flight temperatures, velocities and trajectories of the droplets or particles in the plasma spray are strongly dependent on the spatial distributions of the plasma jet temperature and velocity. For the simulation, the powder feedstock is defined for a range of diameters between 22 and 125 μm in steps of 1 μm. Thus, when the powder is injected into the torch in a radial direction, the particle behavior in the plasma jet is dependent not only on the plasma flow fields through which it travels, but also on its size. The mechanisms of heat and momentum transfer between plasma and particle govern the spatial trajectory, velocity, temperature and the size distribution on reaching the substrates.

Figures 10 and 11 show the contour distributions of particles in terms of diameter, number of particles (concentration), temperature and velocity at the substrate. The data to plot the contours are produced by processing the FLUENT© output through a FORTRAN© program and mapping the contours onto a substrate. The processing method was based on statistical number averaging. The substrate was firstly divided into a number of cells with the dimension of 1 mm × 1 mm. Particles arriving at each cell were counted and their individual parameters i.e. diameter, temperature and velocity were averaged based on Eq. (20).

$$\text{Number-averaged value for parameter } \phi = \frac{\sum_{i=1}^{i=n_p} \phi_i}{n_\mathrm{p}}, \tag{20}$$

where ϕ represents the particle in-flight parameters, viz. size, temperature and velocity, n_p is the number of particles. Then using the cell by cell data, the contours were plotted.

In the left-hand side of Figs. 10 and 11, the distributions are obtained from the freestream model at the same location as where a substrate would be placed. As for the right-hand side, Figs. 10 and 11 contour plots show the distributions for perpendicular and inclined substrates, respectively.

From the comparison for Figs. 10 and 11, no significant effect of substrate, regardless the angle of inclination on particle parameters distributions is observed. In addition, both the freestream and perpendicular substrate models (Fig. 10) indicate circular area of particle distribution covered by the sprayed particles. As for the inclined substrate, the impacting particles envelope an area of distribution similar to an ellipse, for both the freestream and substrate models, as can be seen in Fig. 11. This is because as previously mentioned, the presence of the substrate affects the plasma characteristics significantly only at short range and in the main the processes of heat and momentum transfer are the same for both freestream and substrate models. The temperature and velocity of particles are not affected despite the changes of plasma characteristics in the vicinity or near-field of substrate.

In Figs. 10(a) and 11(a), larger particles are observed to accumulate at lower portion of plasma jet while smaller particles populate the upper half of substrate. This is caused by particles injected perpendicularly into the plasma jet, thus investing them with an initial downward momentum. The more massive particles have higher initial momentum which enables them to penetrate further into the jet and impact at lower part of the substrate.

The size effect also causes larger particles to have a lower temperature and velocity as can be seen in Figs. 10(c,d) and 11(c,d) respectively. Larger particles have higher surface areas exposed to the gas and the mechanism of momentum transfer but their greater masses require higher amount of momentum from the surrounding plasma gas in order to maintain contain the same increase of velocity as the smaller particles. From dimensional analysis, the surface area is proportional to square of diameter while inertia depends on cube of diameter.

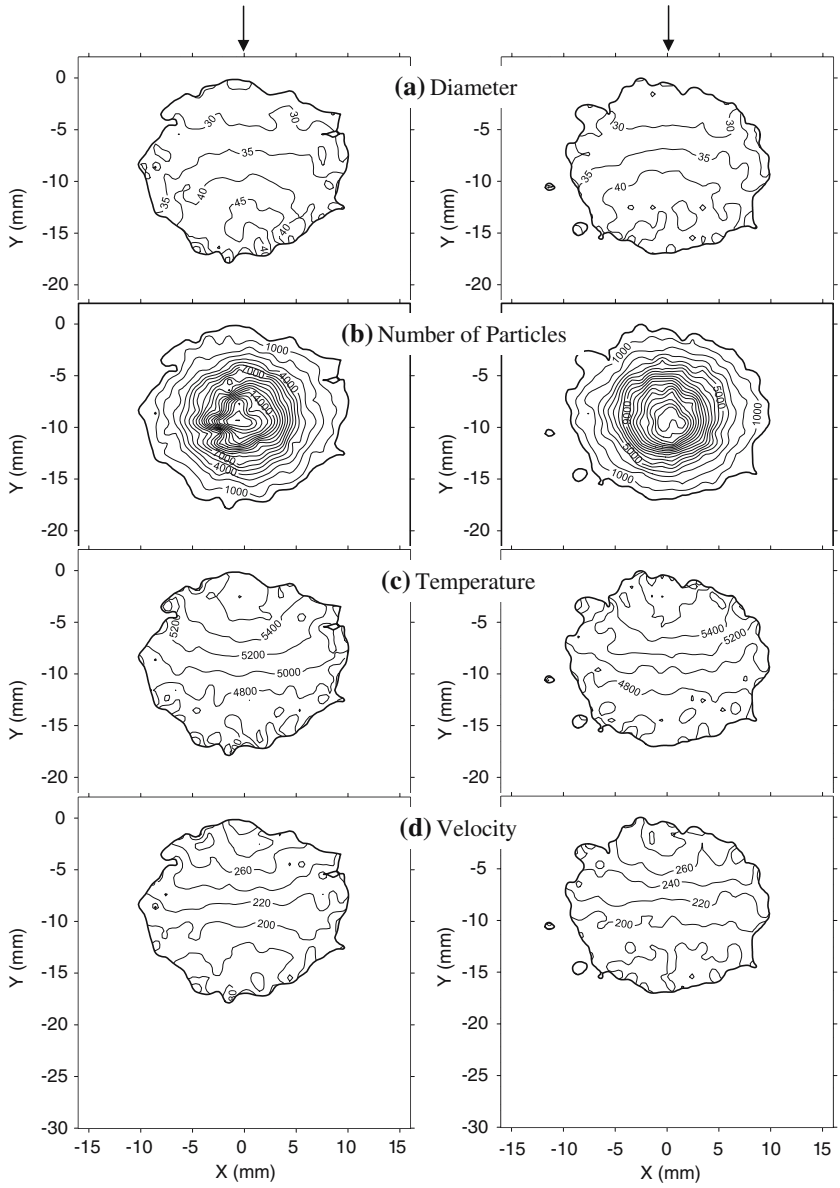

Fig. 10 Comparison of contours of particle in-flight parameters: (**a**) diameter (microns), (**b**) number of particles (n_p), (**c**) surface temperature (K) and (**d**) velocity (m/s) for freestream (left) and perpendicular substrate (right) models. At top of figure, arrows show direction of particle injection at torch

The similar size effect also influences particle heat transfer, in that heat transfer depends on the surface area and the heat capacity is related to the volume. In addition, the degree of penetration in the plasma plume also affects the particle temperature and velocity. By virtue of their greater mass, larger particles penetrate further through the plasma jet and populate the lower periphery of the jet. The environment there has lower temperature and velocity, and

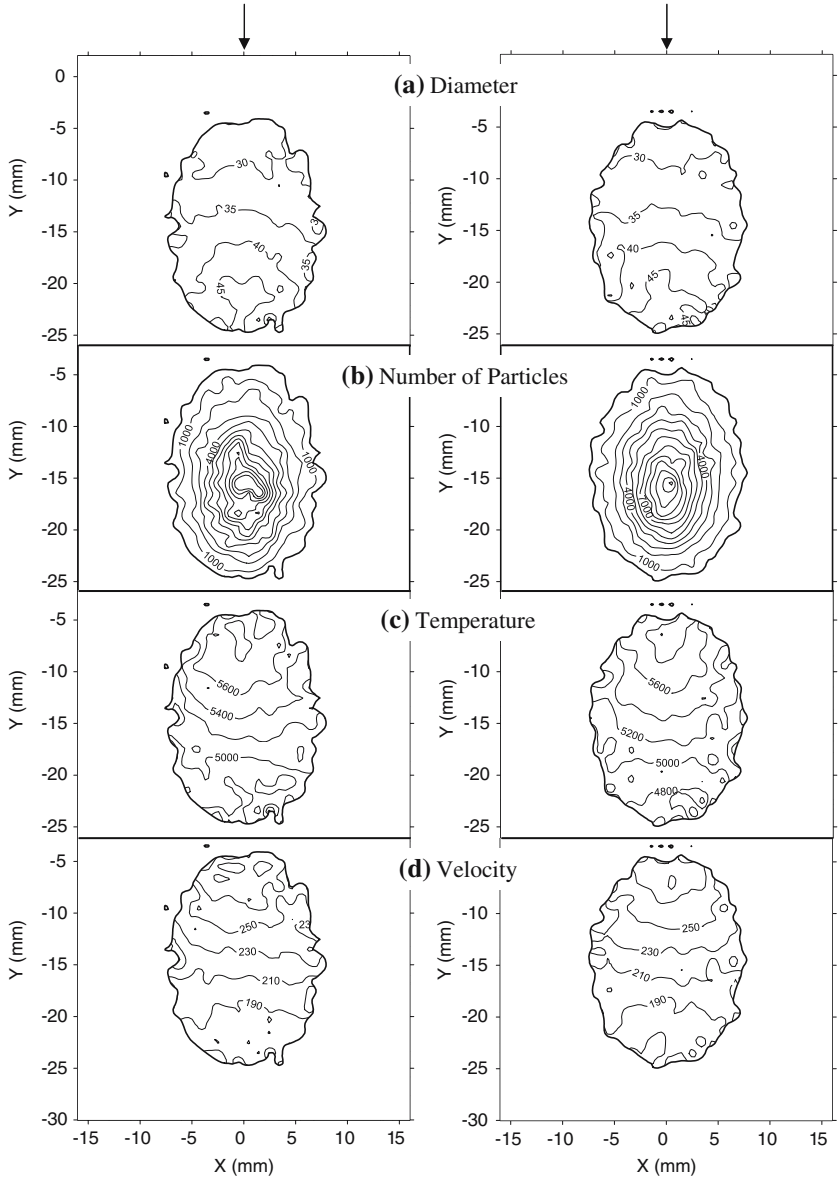

Fig. 11 Comparison of contours of particle in-flight parameters: (**a**) diameter (microns), (**b**) number of particles (n_p), (**c**) surface temperature (K) and (**d**) velocity (m/s) for freestream (left) and inclined substrate (right) models. At top of figure, arrows show direction of particle injection at torch

therefore, larger particles receive lesser heat and momentum compared to smaller particles which reside in the core of the jet.

As a further observation of Figs. 10(c) and 11(c), it is noted that the predicted particle temperature ranges between 4000 and 5400 K. The high temperature with reference to the melting point of 2988 K and boiling point of 5273 K for Zirconia implied that most of the particles would have either melted or vaporized.

In the particle heat transport model, it is assumed that the Biot number is low ($\ll 1.0$). This means that the particle internal heat conduction was more rapid compared to the surface convection from the gas to the surface of particle. The instantaneous heat flow from the surface to the center of the particles gives it the uniform temperature distribution with the particle. This assumption is more valid for metallic particles, but is less so for Zirconia particles.

Zirconia particles have moderate internal thermal resistances, which would result in a lower internal temperature compared to the surface of the particle. Therefore, the predicted particle temperatures which are above vaporization or melting point, may be correct at the surface only and it cannot be presumed the same temperatures exist internally. Therefore, the particle temperature mentioned should be more appropriately referred as the surface temperature of a particle.

As the temperatures predicted are only applicable for the surfaces of the particles, the internal cores of the particles may be at lower temperatures of below melting or boiling points. Hence, it may be imagined that the particle has a solid core surrounded by a molten surface or a liquid core with a boiling surface. At such high surface temperature, there would be loss of mass due to vaporization and this may be one of the factors causing rather low deposition efficiency ($\approx 40\%$) in the actual spraying process using the same operating conditions. There are other factors such as particle losses due to rebound and overspray at substrate which are more dominant in affecting the deposition efficiency. However, the authors believe that the qualitative conclusion; i.e. the insignificant effect of substrate on particle temperature should also hold for model taking internal conduction into consideration, although the numerical results of particle temperature may change.

5. Imaging experiment and results

The SprayWatch© system, supplied by Oseir Ltd. (Hermiankatu, 6 A, 33720 Tampere, Finland) was used to capture the images of in-flight particles as well as measure their temperature and velocity. In this equipment, particle temperature measurement is based on two-color pyrometry principle while time of flight method is used to measure particle velocity.

The SprayWatch© CCD camera was rigidly mounted on the traverse system and placed perpendicularly to the spray plume as shown in Fig. 12. The target area with size of 21.2×25.4 mm and 6 mm depth of field was focused on the torch centerline and stand-off distance of 80 mm away from nozzle front face. When a substrate is present, the deposit is built-up within seconds. The mound like deposit if allowed to grow will divert particles' trajectories and impact locations. In the experiments, this was avoided by continuously feeding the substrate across the plume to expose new area to the spray.

Images of in-flight particles in three cases, i.e. freestream, with perpendicular and inclined substrates were obtained. Figure 13(a–c) shows the streaks of particles flowing through the target areas in the cases of freestream, with perpendicular and inclined substrates, respectively.

Comparing the images, it can be seen that the streams of hot particles traveling in the plasma plume have the similar trajectories. At closer to the substrate surface, the particles impact directly on the substrate without showing any signs of changing their course. This indicates that after being propelled from the torch, the particles with perpendicular and inclined substrates present will receive heat and momentum at the same rate as in the freestream condition. Consequently, in-flight particle temperatures and velocities remain unaffected by the substrate.

6. Conclusions

Numerical and experimental studies had been carried out to investigate the changes of plasma flow fields and particle behavior under the influence of inclined substrates. From numerical investigations, it was found that the existence of the substrates affected the plasma flow fields in the vicinity or near-field of the substrate. The area of influence was small, approximately within 5 mm in front of the substrate surface. However, the distributions of particle parameters, such as size, number concentration, temperature and velocity obtained from the models with substrate were unaffected and remained similar to the freestream condition. The main reason for this was that the particles traveled with such high momentum that their trajectories could not be altered by the plasma flow fields just before impact. It was confirmed experimentally that particles from the freestream condition or with perpendicular and inclined substrate flew with high momentum in the plasma plume. No sudden change in the particles' trajectories was noticed in the images at close proximity of the substrate surface. This finding, i.e. the insignificant effect of the substrate on particle characteristics of size, velocity, temperature, dispersion behavior confirms that the traditional practice of using freestream condition is adequate for most types of plasma spray modeling work.

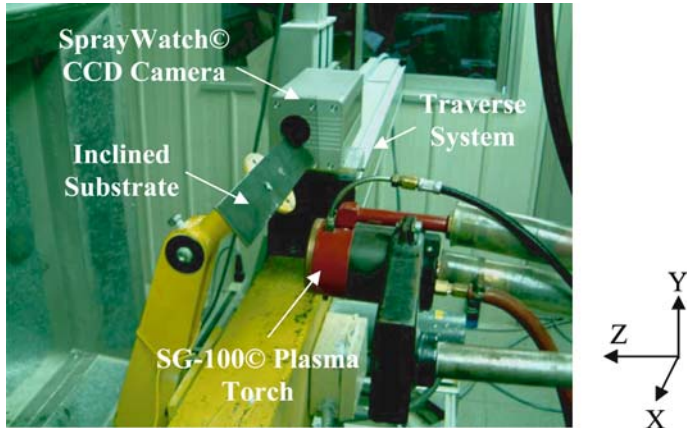

Fig. 12 Experiment setup showing the torch, SprayWatch© camera and traverse system

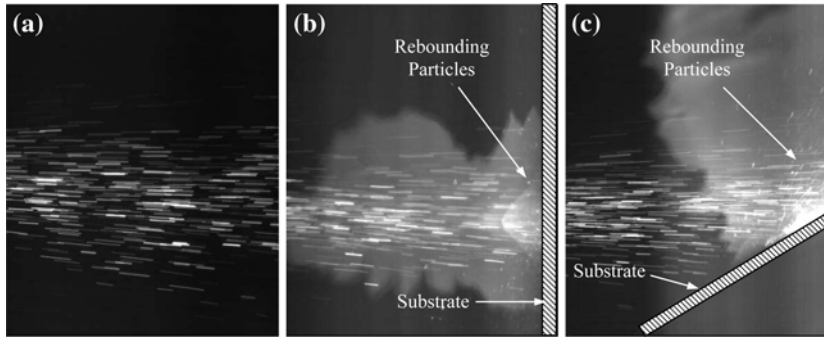

Fig. 13 Images of particles flow in (**a**) freestream, (**b**) with perpendicular and (**c**) inclined substrates present conditions

Acknowledgments The first author (C.W. Kang) is indebted to Nanyang Technological University (NTU), Singapore for the award of his research scholarship.

Appendix A

Calculation of Mach Numbers Inside and Outside the Torch
Inside the torch where the maximum plasma temperature is 11660 K and the maximum plasma velocity is 1115.07 m/s

The specific heat capacity of argon gas, C_p is 3708.62 J/kg K and the gas constant, R is 208.12 J/kg K.

$$\begin{aligned} C_v &= C_\mathrm{p} - R \\ &= 3708.62 - 208.12 = 3500.50\,\mathrm{J/kg\,K} \\ \gamma &= \frac{C_\mathrm{p}}{C_v} = \frac{3708.62}{3500.50} = 1.0595 \end{aligned}$$

$$\text{Sonic velocity} = \sqrt{\gamma RT} = \sqrt{(1.0595)(208.12)(11660)} = 1603.47\,\mathrm{m/s}$$

$$\text{Mach number} = \text{max velocity/sonic velocity} = 1115.07/1603.47 = 0.70 < 1.$$

Since the calculated Mach number is less than 1, it is appropriate to assume the flow is incompressible.
Outside the torch where the maximum plasma temperature is 11641 K and the maximum plasma velocity is 1090.74 m/s

The specific heat capacity of argon gas, C_p is 3671.09 J/kg K and the gas constant, R is 208.12 J/kg K.

$$\begin{aligned} C_v &= C_\mathrm{p} - R \\ &= 3671.09 - 208.12 = 3462.97\,\mathrm{J/kg\,K}, \\ \gamma &= \frac{C_\mathrm{p}}{C_v} = \frac{3671.09}{3462.97} = 1.0601. \end{aligned}$$

$$\text{Sonic velocity} = \sqrt{\gamma RT} = \sqrt{(1.0601)(208.12)(11641)} = 1602.64\,\mathrm{m/s}$$

$$\text{Mach number} = \text{max velocity/sonic velocity} = 1090.74/1602.64 = 0.68 < 1$$

Again, the Mach number is less than 1, the flow is assumed as incompressible.

Appendix B

Derivation of General Form of Governing Differential Equation for Plasma Flow

The rate of change of x-momentum of the fluid element equals the total force in the x-direction on the element due to surface stresses and the rate of increase of x-momentum due to sources; the x-component of the momentum equation is as follows:

$$\frac{\partial(\rho u)}{\partial t} + \nabla.(\rho \boldsymbol{u} u) = \frac{\partial(-p + \tau_{xx})}{\partial x} + \frac{\partial \tau_{yx}}{\partial y} + \frac{\partial \tau_{zx}}{\partial z} + S_{Mx}. \tag{A.1}$$

In a Newtonian fluid, the viscous stresses are proportional to the rates of deformation. In the case of incompressible flow, the nine viscous stress components, of which six are independent, are:

$$\tau_{xx} = 2\mu \frac{\partial u}{\partial x}, \tag{A.2}$$

$$\tau_{yy} = 2\mu \frac{\partial v}{\partial y}, \tag{A.3}$$

$$\tau_{zz} = 2\mu \frac{\partial w}{\partial z}, \tag{A.4}$$

$$\tau_{xy} = \tau_{yx} = \mu \left(\frac{\partial u}{\partial y} + \frac{\partial v}{\partial x} \right), \tag{A.5}$$

$$\tau_{xz} = \tau_{zx} = \mu \left(\frac{\partial u}{\partial z} + \frac{\partial w}{\partial x} \right), \tag{A.6}$$

$$\tau_{yz} = \tau_{zy} = \mu \left(\frac{\partial v}{\partial z} + \frac{\partial w}{\partial y} \right). \tag{A.7}$$

Substituting Eqs. (A.2) to (A.7) into Eq. (A.1) gives

$$\frac{\partial(\rho u)}{\partial t} + \nabla \cdot (\rho \boldsymbol{u} u) = -\frac{\partial p}{\partial x} + \frac{\partial}{\partial x}\left(2\mu \frac{\partial u}{\partial x}\right) + \frac{\partial}{\partial y}\left[\mu \left(\frac{\partial u}{\partial y} + \frac{\partial v}{\partial x} \right)\right] + \frac{\partial}{\partial z}\left[\mu \left(\frac{\partial u}{\partial z} + \frac{\partial w}{\partial x} \right)\right] + S_{Mx}, \tag{A.8}$$

$$\frac{\partial(\rho u)}{\partial t} + \nabla \cdot (\rho \boldsymbol{u} u) = -\frac{\partial p}{\partial x} + \frac{\partial}{\partial x}\left(\mu \frac{\partial u}{\partial x}\right) + \frac{\partial}{\partial y}\left(\mu \frac{\partial u}{\partial y}\right) + \frac{\partial}{\partial z}\left(\mu \frac{\partial u}{\partial z}\right) + \left[\frac{\partial}{\partial x}\left(\mu \frac{\partial u}{\partial x}\right) + \frac{\partial}{\partial y}\left(\mu \frac{\partial v}{\partial x}\right) + \frac{\partial}{\partial z}\left(\mu \frac{\partial w}{\partial x}\right)\right] + S_{Mx} \tag{A.9}$$

$$\frac{\partial(\rho u)}{\partial t} + \nabla.(\rho \boldsymbol{u} u) = -\frac{\partial p}{\partial x} + \nabla.(\mu \nabla u) + S_{Mx}. \tag{A.10}$$

For a steady, turbulent flow and without additional source to increase the momentum in x-direction, Eq. (A.10) can be rewritten as

$$\nabla.(\rho \boldsymbol{u} u) = \nabla.[(\mu_l + \mu_t)\nabla u] - \frac{\partial p}{\partial x} \tag{A.11}$$

Comparing Eq. (A.1l) with the general form of governing equation given in Eq. (1),

$$\nabla \cdot (\rho \boldsymbol{u} \phi) = \nabla \cdot (\Gamma_\phi \nabla \phi) + S_\phi \tag{1}$$

the diffusion coefficient, Γ_ϕ equals $\mu_l + \mu_t$ and the source term contains $-\frac{\partial p}{\partial x}$.

References

1. Fauchais P, Vardelle A, Dussoubs B (2001) Thermal spray 2001: New surfaces for a New Millennium, Materials Park, Ohio, USA, p 1
2. Fauchais P (2004) J Phys D Appl Phys 37: 86
3. Huang PC, Heberlein J, Pfender E (1995) Surf Coat Tech, 73:142
4. Jog MA, Huang L (1996) J Heat Trans-T ASME 118:471
5. Wan YP, Prasad V, Wang G-X, Sampath S, Fincke JR (1999) J Heat Trans-T ASME 121:691
6. Dussoubs B, Fauchais P, Vardelle A, Vardelle M, Themelis NJ (1997) Thermal Spray: A United Forum for Scientific and Technological Advances, USA 557
7. Li H, Chen X (2002) Plasma Chem Plasma P 22(1):27
8. Xiong HB, Zheng LL, Sampath S, Williamson RL, Fincke JR (2004) Int J Heat Mass Tran 47:5189
9. Zhang T, Gawne DT, Liu B (2000) Surf Coat Technol 132:233

10. Ahmed I, Bergman TL (2000) J Therm Spray Technol 9(2):215
11. Ahmed I, Bergman TL (2001) J Heat Trans-T ASME 123:188
12. Williamson RL, Fincke JR, Chang CH (2002) J Therm Spray Technol 11(1):107
13. Nylén P, Friis M, Hansbo A, Pejryd L (2001) J Therm Spray Technol 10(2):359
14. Remesh K, Ng HW, Yu SCM (2003) J Therm Spray Technol 12(3):377
15. Remesh K, Yu SCM, Ng HW, Berndt CC (2003) J Therm Spray Technol 12(4):508
16. Lapierre D, Kearney RJ, Vardelle M, Vardelle A, Fauchais P (1994) Plasma Chem Plasma P 14(4):407
17. Boulos MI, Fauchais P, Pfender E, (1994) Thermal plasmas: fundamentals and applications, Plenum Press, New York
18. Ang CB, Ng HW, Yu SCM, Lam YC (2000) Plasma Chem Plasma P 20(3):325
19. Launder BE, Spalding DB (1974) Comput Method Appl M 3:269
20. FLUENT Inc. (2001) FLUENT user's guide, Lebanon, NH 03766
21. Petukhov BS, Polyakov AF (1988) Heat transfer in turbulent mixed convection, Hemisphere Publishing Corporation, USA. p 27
22. Jayatilleke C (1969) Progress in heat and mass transfer: the influence of Prandtl number and surface roughness on the resistance of the laminar sublayer to momentum and heat transfer, Pergamon Press, New York, p 193
23. Patankar SV (1980) Numerical heat transfer and fluid flow, Hemisphere Publishing Corporation, Washington, DC
24. Versteeg HK, Malalasekera W (1995) An introduction to computational fluid dynamics - The finite volume method, Longman Scientific and Technical, England
25. Ang CB, Devasenapathi A, Ng HW, Yu SCM, Lam YC (2001) Plasma Chem Plasma P 21(2):401
26. Ranz WE, Marshall WR (1952) Chem Eng Prog 48(3):141 (1952).
27. Murphy AB, Kovitya P (1993) J Appl Phys 73(10):4759